https://doi.org/10.1016/j.jallcom.2018.09.224

Enhancing high-voltage performance of $LiNi_{0.5}Co_{0.2}Mn_{0.3}O_2$ cathode material via surface modification with lithium-conductive $Li_3Fe_2(PO_4)_3$

Bin Huang[†,‡], Guangzhe Li[†], Zhefei Pan[†], Xiangyu Su[†], Liang An[†,*]

[†] Department of Mechanical Engineering, The Hong Kong Polytechnic University, Hung Hom, Kowloon, Hong Kong SAR, China

[‡] Guangxi Key Laboratory of Electrochemical and Magneto-chemical Functional Materials, College of Chemistry and Bioengineering, Guilin University of Technology, Guilin, 541004, China

*Corresponding author.

Email: liang.an@polyu.edu.hk (L. An)

Abstract: Increasing Ni content and (or) elevating the upper cut-off operating voltage are the most frequently utilized methods for enhancing the energy density of Ni-based layered cathode materials in lithium-ion batteries. However, both methods will lead to the structure instability and aggravate the unwanted side reactions between electrode and electrolyte. Aiming at mitigating this problem, lithium-conductive $Li_3Fe_2(PO_4)_3$ is employed as a coating layer to enhance the high-voltage performance of $LiNi_{0.5}Co_{0.2}Mn_{0.3}O_2$ cathode material for lithium-ion batteries. A homogeneous Li, Fe and P-containing colloidal suspension is prepared, via a facile wet chemical method, and used as the precursor in preparing the coating layer. X-ray diffraction and scanning electron microscope results indicate that the surface coating do not alter the structure and morphology of the material particles. Energy dispersive spectrometry

and elemental mapping results confirm that the coating layer is uniformly distributed on the surface of the matrix material. Electrochemical characterizations demonstrate that all the surface-modified samples exhibit slower capacity fading than the bare one at elevated upper cut-off voltages. For instance, the one with 1.0 wt. % $Li_3Fe_2(PO_4)_3$ coating has a remaining discharge capacity of 135.3 mAh g^{-1} after 100 charge-discharge cycles at 1 C rate upon the voltage range of 2.8-4.5 V, with a capacity retention of 75.33%, whereas the uncoated one exhibits the discharge capacity and the capacity retention of only 91.8 mAh g^{-1} and 51.92%, respectively, under the same experimental conditions. Furthermore, 1.0 wt. % $Li_3Fe_2(PO_4)_3$-coated material shows a film resistance (R_{sf}) of 40.47 Ω and the charge-transfer resistance (R_{ct}) of 35.69 Ω after 100 cycles, whereas the values of the uncoated one are 102.43 Ω and 42.76 Ω, demonstrating that the surface coating can lead to a more stable solid-electrolyte interphase (SEI) layer.

Keywords: Lithium-ion batteries; Layered cathode; Coating; Surface modification; High voltage

1. Introduction

Among electrochemical energy storage systems, lithium-ion batteries (LIBs) have gained great success in the consumer electronics market, and garnered much attention for the use in electric vehicles (EVs) due to its excellent portability, high energy density and long cycling life[1-5]. As for the cathode material, Ni-based layered $Li[Ni_{1-x}M_x]O_2$ (M=Co, Mn, Al, etc.) compounds have been considered as promising candidates for automotive LIBs due to their high energy density[6, 7]. However, with the rapid popularization of EVs, the requirement of mileage on a single charge for EVs is constantly increasing. In order to meet this demand, the specific capacity of Ni-based layered cathode materials can be enhanced by increasing the Ni ratio[8] or elevating the upper cut-off operating voltage[9]. For the Ni-rich $Li[Ni_{1-x}M_x]O_2$ in which x value is no more than 0.2, such as $LiNi_{0.8}Co_{0.1}Mn_{0.1}O_2$ and $LiNi_{0.8}Co_{0.15}Al_{0.05}O_2$, the cation mixing, thermal instability, and surface side reactions with electrolyte caused by the chemical instable Ni^{3+} and Ni^{4+} contribute to the severe capacity fading[10-12]. In addition, for the materials cycled at elevated upper cut-off voltage (> 4.2 V), side reactions between electrolytes and the surface of the materials will be aggravated, resulting in the formation of insulating layer on the surface and deteriorated electrochemical performance[13-15]. It has been demonstrated that the structural degradation of Ni-based layered materials begins from the surface region of the material particles where the rhombohedral phase readily transforms into inactive rock salt phases[15, 16]. Therefore, the interfacial stability between electrode material and electrolyte is critical to the cycling life, particularly for the Ni-rich counterparts

and those operated at higher voltage.

Surface modification is an effective way to improving interfacial stability and suppressing the deterioration of electrochemical properties. Various stable oxides, fluorides and phosphates have been employed as coating layers to restrain the side reactions between electrode material and electrolyte, such as Al_2O_3[17, 18], TiO_2[19, 20], ZnO[21], AlF_3[22-24], $FePO_4$[25], $Al(PO_4)_3$[26, 27], etc. However, most of the coating materials are inert compounds which may impede the Li^+ transportation between electrode and electrolyte. Thus, in order to eliminate the negative effect of coating layer, some Li-conductive compounds have been proposed as new coating materials[28-31]. For example, Wang et al.[28] used Li_2ZrO_3 as a coating layer to enhance the electrochemical performance of $LiNi_{0.5}Co_{0.2}Mn_{0.3}O_2$. Their results showed that the 1 wt. % Li_2ZrO_3-coated material had significantly improved cycling stability than the bare sample. Moreover, the Li_2ZrO_3 coating could also reduce the polarization and enhance the electrochemical activity of the material. Huang et al.[31] prepared Li_3VO_4-coated $LiNi_{0.5}Co_{0.2}Mn_{0.3}O_2$. The coating layer had important functions of stabilizing the interface between the electrode material and the electrolyte, as well as acting as an excellent Li^+ conductor.

In this work, NASICON-structured $Li_3Fe_2(PO_4)_3$, which has a stable poly-anionic $[Fe_2(PO_4)_3]$ framework[32], is employed as a Li^+-conductive coating layer for suppressing the performance deterioration of $LiNi_{0.5}Co_{0.2}Mn_{0.3}O_2$ at elevated operating voltage. The $Li_3Fe_2(PO_4)_3$-coated $LiNi_{0.5}Co_{0.2}Mn_{0.3}O_2$ (NCM-LFP) is prepared via a facile wet chemical colloidization-annealing process. In this way,

$LiNi_{0.5}Co_{0.2}Mn_{0.3}O_2$ is firstly treated with an ethanol-based colloidal mixture of Li_3PO_4 and $FePO_4$. The subsequent annealing can transform the colloidal mixture into $Li_3Fe_2(PO_4)_3$ which homogeneously disperses on the surface of the matrix particles. As a result, the electrochemical properties of the material at elevated operating voltage are much improved.

2. Experimental

The $Ni_{0.5}Co_{0.2}Mn_{0.3}(OH)_2$ precursor was obtained from commercial supply. The bare $LiNi_{0.5}Co_{0.2}Mn_{0.3}O_2$ was synthesized as following. The precursor and Li_2CO_3 were mixed in a molar ratio of 1:1.05 and thoroughly ground, followed by annealing at 500 ^oC for 5 hours and 900 ^oC for 15 hours, sequentially.

To coat the bare $LiNi_{0.5}Co_{0.2}Mn_{0.3}O_2$ with $Li_3Fe_2(PO_4)_3$, a colloidal mixture of Li_3PO_4 and $FePO_4$ was firstly prepared as following. Stoichiometric $Fe(NO_3)_3 \cdot 9H_2O$ and CH_3COOLi were dissolved in a mixture of 20 mL ethanol and 5 mL glycol to form an orange-red solution. Then appropriate amount of $NH_4H_2PO_4$ was dissolved in distilled water to form clear solution. Subsequently, $NH_4H_2PO_4$ solution was added into the orange-red solution with vigorous stirring to form a light-yellow colloidal solution (shown in Fig. S1). After that, 5 g as-prepared $LiNi_{0.5}Co_{0.2}Mn_{0.3}O_2$ was dispersed into the colloidal solution with stirring for 30 min. The Li_3PO_4 and $FePO_4$ co-coated powder was filtered and washed with ethanol several times, followed by an annealing at 650 ^oC for 3 hours. The weight ratio of coating layer was varied as 0, 0.5, 1, 2, and 3 wt. %, and the corresponding samples were marked as NCM-LFP0, NCM-LFP0.5, NCM-LFP1, NCM-LFP2 and NCM-LFP5, respectively.

X-ray diffraction (XRD) patterns were measured using a Rigaku Rint-2000 diffractometer with Cu-Kα radiation (1.54056Å). The morphologies of the as-prepared samples were observed by a scanning electron microscope (SEM, Hitachi, SU5000). Moreover, X-ray photoelectron spectroscopy (XPS, Thermo Fisher Scientific ESCALAB 250Xi) measurements were performed to get information on the surface of the materials.

CR 2016 coin-type cells were assembled with metallic lithium as counter electrodes for electrochemistry studies. Each working electrode was composed of 80 wt. % as-prepared sample, 10 wt. % Super P carbon black and 10 wt. % poly(vinylidene fluoride). The cells were assembled in an Ar-filled glove box (Mikrouna) and tested using galvanostatic mode at a desired C rate (1 C corresponds to 160 mA g^{-1}). Electrochemical impedance spectroscopy (EIS) was also carried out after different cycle numbers. The sinusoidal excitation voltage applied to the cells was 5 mV with a frequency range of between 0.01 Hz to 100 kHz.

3. Results and discussion

3.1 Physical characterizations

The XRD patterns of the as-prepared samples are shown in Fig. 1, in which it can be seen that all the samples are hexagonal α-$NaFeO_2$ structure ($R\bar{3}m$ space group). The peak splits of (006)/(102) and (108)/(110) can be clearly observed, indicating the formation of highly ordered layered structure. The diffraction peaks of $Li_3Fe_2(PO_4)_3$ can hardly be detected in the NCM-LFP0.5, NCM-LFP1 and NCM-LFP2 samples. However, in the NCM-LFP3 sample, the observed trace signal ranging from 19°~30°

can be indexed to $Li_3Fe_2(PO_4)_3$ (JCPDS card No. 78-1106). In addition, the XRD pattern of the pure $Li_3Fe_2(PO_4)_3$ is given in Fig. S2. The values of lattice constants *a* and *c* calculated based on the XRD patterns of the as-prepared samples are listed in Table 1, indicating that no significant structural change in the materials is detected after coating. With the increase of the coating amount, the *c*/*a* value increases slightly, suggesting that the surface coating could lead to cation mixing in the layered hexagonal structure [12]. That is ascribed to the heteroatoms penetration by the coating layer[20, 33].

Fig. 2 shows the SEM images of the as-prepared samples. The SEM images collected in different magnifications of the bare sample are shown in Fig. 2a-c. It can be seen that the material particles are quasi-spherical with a diameter of about 10 μm, and composed of nanoscale primary particles (Fig. 2a and b). In Fig. 2c we can observe the smooth skin of the bare particle, without any impurities. Fig. 2d-o exhibit the SEM images of the $Li_3Fe_2(PO_4)_3$-coatd samples, which indicate that the shape and size are not altered by the coating layer. However, the surface morphology of the coated samples is obviously different from that of the bare one. In Fig. 2f, i, l and o it can be seen that the NCM-LFP0.5, NCM-LFP1, NCM-LFP2 and NCM-LFP3 have rough surface, which is caused by the coating layer.

The existence of coating layer can be further confirmed by the energy dispersive spectrometry (EDS) results, which are shown in Fig. 3 and 4. Fig. 3 shows the EDS elemental mappings for Fe and P of the $Li_3Fe_2(PO_4)_3$-coatd samples. For the samples NCM-LFP0.5 and NCM-LFP1, Fe and P are homogeneously dispersed on the surface

of the material particles, suggesting the uniform distribution of $Li_3Fe_2(PO_4)_3$ (Fig. 3b, c, e and f). By contrast, some areas with condensed signals can be observed in the results of NCM-LFP2 and NCM-LFP3 (Fig. 3h, i, k and l). The reason for this phenomenon is the aggregation of the coating material. Moreover, the EDS spectra of all the as-prepared samples are given in Fig. 4. The regions from which the EDS spectra were collected are shown in Fig. S3. In Fig. 4b-e we can clearly see Fe and P signals, and that the peak intensities of them increase as the amount of coating layer increases. Additionally, the results of the semi-quantitative analysis for Fe and P are shown in Fig. 4f. Both of them trend to increase from NCM-LFP0 to NCM-LFP3, in the meanwhile, the detected weight fractions are roughly consistent with the designed value.

Fig. 5 shows the XPS spectra of the bare and the 1 wt. % $Li_3Fe_2(PO_4)_3$-coated $LiNi_{0.5}Co_{0.2}Mn_{0.3}O_2$. As shown in Fig. 5a, b and c, the peak positions of Ni 2p, Co 2p and Mn 2p of the NCM-LFP1 are in consistent with those of the bare sample, suggesting that the coating layer does not alter the valence states of the transition metals in the material. The binding energy of Ni $2p_{3/2}$ is 854.6 eV, revealing that the oxidation state of Ni is a mixture of Ni^{2+} and Ni^{3+}; meanwhile, the peaks of Co $2p_{3/2}$ and Mn $2p_{3/2}$ are at 780.0 eV and 642.2 eV, respectively, indicating that the oxidation states of Co and Mn in the material are Co^{3+} and Mn^{4+}[12, 28]. Fig. 5d shows the Fe 2p spectrum of the NCM-LFP1, in which two peaks located at 724.5 eV (Fe $2p_{1/2}$) and 711.1 eV (Fe $2p_{3/2}$). The result confirms that the valence state of Fe in the modified sample is Fe^{3+}[34, 35]. In addition, the binding energy of P 2p in the NCM-LFP1 is

133.1 eV, which is consistent with the value of $[PO_4]^{3-}$ group[36, 37], as shown in Fig. 5e. What is worth mentioning is that the C 1s peak located at 289.6 eV, corresponding to Li_2CO_3[38], for the NCM-LFP1 is significantly lower than that for the NCM-LFP0 (Fig. 5f). The result suggests that the NCM-LFP1 has less "lithium residue" on its surface than the NCM-LFP0.

3.2 Electrochemical characterizations

In this section, comparative studies on electrochemical properties of the as-prepared materials under overcharge conditions are exhibited and discussed. The results of the initial galvanostatic charge-discharge (0.1 C) curves tested within different operating voltage windows are shown in Fig. 6a and b. When operated between 2.8 and 4.5 V, as can be seen in Fig. 6a, the bare material delivers initial charge and discharge capacities of 221.8 and 189.1 mAh g^{-1}, with the coulombic efficiency of 85.26%. The other samples have slightly lower capacities than the bare one. We can clearly see that the discharge capacities of NCM-LFP0.5, NCM-LFP1, NCM-LFP2 and NCM-LFP3 are 185.3, 186.0, 184.2 and 177.6 mAh g^{-1}, respectively, and the corresponding coulombic efficiencies are 84.50%, 85.91%, 80.79% and 79.21%. Fig. 6b shows the initial charge-discharge curved tested between 2.8 and 4.6 V. It can be seen that the NCM-LFP0, NCM-LFP0.5, NCM-LFP1, NCM-LFP2 and NCM-LFP3 exhibits discharge capacities of 199.9, 195.3, 193.2, 190.7 and 182.2 mAh g^{-1}, with the coulombic efficiencies of 81.46%, 85.10%, 86.33%, 82.00% and 80.76%, respectively.

As mentioned above, it is well known that elevating the upper cut-off voltage can

improve energy density for layered cathode materials. Thus, all the as-prepared samples deliver higher specific capacities within 2.8-4.6 V than within 2.8-4.5 V. However, the Ni^{3+} and Ni^{4+} in the delithiated materials will oxidize the electrolyte molecules which are in contact with the surface of the materials[25, 39]. Moreover, it has been demonstrated that the Ni^{2+}/Ni^{3+} and Ni^{3+}/Ni^{4+} redox couples had a catalyst function during charge process, which could facilitate electrolyte decomposition at the interphase between electrode and electrolyte[40, 41]. These side reactions between electrode and electrolyte can be the main origin of the irreversible capacity loss during initial charge-discharge, as well as the reason why the bare sample has lower initial coulombic efficiency at the upper cut-off voltage of 4.6 V than at that of 4.5 V. It has been widely reported that surface coating could suppress these side reactions, and Fig. 6a and b indicate that the NCM-LFP1 sample exhibits the highest initial coulombic efficiency. However, this value decreases with the increase of the amount of the coating layer. In other words, excess coating layer may cause inferior coulombic efficiency. Many research groups have reported this phenomenon, which is in agreement with our results [20, 29, 33, 42, 43], but they did not explain the reason in detail. To our best knowledge, excess amount of coating layer may bring some negative effects. For example, some elements in the coating layer may penetrate into the cathode particles and lead to cation mixing during the synthesis, consequently resulting in lower initial coulombic efficiency and deteriorated cycling stability. This was demonstrated by the XRD results, as well as Li et al.'s studies [20, 33].

What is worth mentioning is that the $Li_3Fe_2(PO_4)_3$-coated materials have slightly

lower capacities than the bare one, since the coating material can hardly be lithiated within the operating voltage range for $LiNi_{0.5}Co_{0.2}Mn_{0.3}O_2$[44, 45]. With the different amount of coating layer, the material will have different theoretical capacities. However, the theoretical capacities of layered cathode materials (e.g. $LiCoO_2$, $LiNi_xCo_yMn_zO_2$, $LiNi_xCo_yAl_zO_2$, etc.) cannot be achieved in practice, since the crystal structures will be changed irreversibly if all the Li-ions are extracted. In fact, nominal capacities are usually used as the benchmark for this type of cathode materials. Hence, the nominal capacity of $Li_3Fe_2(PO_4)_3$-coated $LiNi_{0.5}Co_{0.2}Mn_{0.3}O_2$ will decrease as the amount of coating layer increases. Fig. 6a and b show that the trend of the achievable capacities of the as-prepared samples is consistent with this rule.

Fig. 6c and d show the cycling performances of the as-prepared samples tested at 1 C rate within the operating voltage windows of 2.8-4.5 V and 2.8-4.6 V. It can be seen that the bare material shows the fastest capacity fading, both at the two upper cut-off voltages. By contrast, the $Li_3Fe_2(PO_4)_3$-coated materials show improved stability than the bare one. Among these samples, NCM-LFP1 displays the best cycling performance. Within the voltage range of 2.8-4.5 V, as shown in Fig. 6c, NCM-LFP1 delivers a discharge capacity of 179.6 mAh g^{-1} at the first cycle and that of 135.3 mAh g^{-1} at the 100^{th} cycle, with the capacity retention of 75.33%; whereas NCM-LFP0 has the discharge capacities of 176.8 and 91.8 mAh g^{-1} at the 1^{st} and 100^{th} cycles, respectively, with the retention of 51.92%. When the upper cut-off voltage is elevated to 4.6 V, the discharge capacities of NCM-LFP0 at 1^{st} and 100^{th} cycles are 180.3 and 60.5 mAh g^{-1}, respectively; the corresponding capacity retention is only 33.56%, as

shown in Fig. 6d. For NCM-LFP1, however, the two values are 183.9 and 125.6 mAh g^{-1}, with the capacity retention of 68.30%. It is worth noting that NCM-LFP2 and NCM-LFP3 show slightly lower capacity retentions than NCM-LFP1. It may be ascribed to the aforementioned negative effects brought by the excess amount of coating layer. Even so, it is reasonable to conclude that the $Li_3Fe_2(PO_4)_3$ coating layer can suppress the capacity fading for $LiNi_{0.5}Co_{0.2}Mn_{0.3}O_2$ during cycling tests.

To further investigate the kinetics of charge transport, EIS measurements were carried out on the as-prepared samples. The data was collected after the 1st and the 100th charge-discharge cycle at 1 C rate. Before the measurements, all of the cells were charged to 4.0 V for obtaining an identical status. The results are shown in Fig. 7. Each Nyquist plot has one high-frequency semicircle, one medium-frequency semicircle and one low-frequency tail, which are related to the surface film resistance (R_{sf}), the charge-transfer resistance (R_{ct}) and the Warburg impedance (Z_w), respectively[46]. The obtained Nyquist plots are simulated using the equivalent circuit shown in Fig. 7f, and the calculated values of the parameters are listed in Table 2. It can be seen that NCM-LFP0 has relatively lager R_{sf} and R_{ct} values after 100 charge-discharge cycles. Moreover, the R_{sf} of NCM-LFP0 goes up to a large value, 78.85 Ω, after the first cycling, suggesting that this cell has had a severe electrolyte decomposition during the first charging. With the surface coating, the value of R_{sf} decreases significantly. That is attributed to the more stable SEI layer on the surface-coated samples. Therefore, the $Li_3Fe_2(PO_4)_3$ coating layer can suppress the thickening of the solid-electrolyte interphase (SEI) film during cycling, which is the

main reason for the increasing of R_{sf}[47, 48]. However, continuing increase in the amount of the coating layer leads to an increasing R_{ct} value, as shown in Fig. 7d and e, suggesting that the charge-transfer kinetics would be hindered by the excess amount of surface coating.

The function of the $Li_3Fe_2(PO_4)_3$ coating layer as a Li-conductive protector is illustrated in Fig. 8. Fig. 8a describes the coating process, through which a uniform coating layer can be formed on the surface of the cathode material. Without surface coating, as shown in Fig. 8b, the trace HF in the electrolyte will attack and corrode the surface of the material particles, leading to the dissolution of transition metals and accumulation of inactive fluorides. In addition, side-reactions between electrode and electrolyte during charge-discharge cycles, particularly at elevated upper cut-off voltages, cause continuous formation of SEI layer. These may be the main reason for the increase of the resistance and the fast capacity fading. When the material is coated with $Li_3Fe_2(PO_4)_3$, the HF attack and side-reactions can be remarkably excluded, as shown in Fig. 8c. In the meanwhile, Li^+ transportation between the cathode material and the electrolyte will not be broken off due to the Li-conductive nature of the coating layer. Therefore, the $Li_3Fe_2(PO_4)_3$-coated sample has improved cycling stability at elevated upper cut-off voltages and lower resistance after charge-discharge cycles. It is worth mentioning that the relation between capacity fading and the dissolution of Ni, Co and Mn from the material has not been investigated in this work, but it is very important for further elucidating the mechanism of performance degradation and the protective effect of the coating layer. In addition, the ions derived

from the dissolution of the coating layer may have impacts on the performance of the cell. Hence, the relation between the performance degradation and the metal ions dissolved in the electrolyte will be investigated in our following work.

4. Concluding remarks

NASICON-structured $Li_3Fe_2(PO_4)_3$-coated $LiNi_{0.5}Co_{0.2}Mn_{0.3}O_2$ cathode materials have been successfully synthesized through a facile wet chemical process. Based on XRD and SEM measurements, we know that the coating layer has no significant impact on the structure and morphology of the matrix material. The EDS and EDS mappings indicate that the coating material can be uniformly dispersed on the surface of the cathode particles by our coating method. The significantly improved electrochemical properties at elevated upper cut-off voltages are attributed to the stable Li^+-conductive $Li_3Fe_2(PO_4)_3$. Not only can the coating layer protect the cathode material, but also provides diffusion paths between the electrode and electrolyte for Li^+. By taking the advantages of the coating layer, all the surface-modified samples exhibit slower capacity fading than the bare one at elevated upper cut-off voltages. Particularly, the one with 1 wt. % $Li_3Fe_2(PO_4)_3$ coating shows the best electrochemical performance. In addition, the 1 wt. % $Li_3Fe_2(PO_4)_3$-coated material has more stable SEI layer than the bare one. Furthermore, this method can be used as an effective way to preparing other Ni-based materials for high voltage LIBs.

Acknowledgements

This work was supported by a grant from Guangxi Natural Science Foundation

(2017GXNSFBA198141) and a grant from the Research Grants Council of the Hong Kong Special Administrative Region, China (Project No. 25211817).

References

[1] L. An, C.Y. Jung, Applied Energy, 205 (2017) 1270-1282.

[2] Q.X. Wu, Z.F. Pan, L. An, Renewable and Sustainable Energy Reviews, 89 (2018) 168-183.

[3] Z.F. Pan, L. An, T.S. Zhao, Z.K. Tang, Progress in Energy and Combustion Science, 66 (2018) 141-175.

[4] A. Khor, P. Leung, M.R. Mohamed, C. Flox, Q. Xu, L. An, R.G.A. Wills, J.R. Morante, A.A. Shah, Materials Today Energy, 8 (2018) 80-108.

[5] Y. Yu, X. Yang, Y. Zhao, X. Zhang, L. An, M. Huang, G. Chen, R. Zhang, Angewandte Chemie, 130 (2018) 8686-8690.

[6] S. Liu, C. Zhang, Q. Su, L. Li, J. Su, T. Huang, Y. Chen, A. Yu, Electrochimica Acta, 224 (2017) 171-177.

[7] J.-M. Lim, T. Hwang, D. Kim, M.-S. Park, K. Cho, M. Cho, Scientific Reports, 7 (2017) 39669.

[8] A. Manthiram, J.C. Knight, S.T. Myung, S.M. Oh, Y.K. Sun, Advanced Energy Materials, 6 (2016) 1501010.

[9] C.-H. Shen, Q. Wang, H.-J. Chen, C.-G. Shi, H.-Y. Zhang, L. Huang, J.-T. Li, S.-G. Sun, ACS Applied Materials & Interfaces, 8 (2016) 35323-35335.

[10] D.-J. Lee, B. Scrosati, Y.-K. Sun, Journal of Power Sources, 196 (2011)

7742-7746.

[11] H.S. Liu, Z.R. Zhang, Z.L. Gong, Y. Yang, Electrochemical and Solid-State Letters, 7 (2004) A190-A193.

[12] B. Huang, X. Li, Z. Wang, H. Guo, L. Shen, J. Wang, Journal of Power Sources, 252 (2014) 200-207.

[13] D. Wang, X. Li, Z. Wang, H. Guo, Y. Xu, Y. Fan, Electrochimica Acta, 196 (2016) 101-109.

[14] J. Li, L.E. Downie, L. Ma, W. Qiu, J.R. Dahn, Journal of The Electrochemical Society, 162 (2015) A1401-A1408.

[15] F. Lin, I.M. Markus, D. Nordlund, T.-C. Weng, M.D. Asta, H.L. Xin, M.M. Doeff, Nature Communications, 5 (2014) 3529.

[16] S.-K. Jung, H. Gwon, J. Hong, K.-Y. Park, D.-H. Seo, H. Kim, J. Hyun, W. Yang, K. Kang, Advanced Energy Materials, 4 (2014) 1300787.

[17] Y. Su, S. Cui, Z. Zhuo, W. Yang, X. Wang, F. Pan, ACS Applied Materials & Interfaces, 7 (2015) 25105-25112.

[18] A.M. Wise, C. Ban, J.N. Weker, S. Misra, A.S. Cavanagh, Z. Wu, Z. Li, M.S. Whittingham, K. Xu, S.M. George, M.F. Toney, Chemistry of Materials, 27 (2015) 6146-6154.

[19] Y. Chen, Y. Zhang, B. Chen, Z. Wang, C. Lu, Journal of Power Sources, 256 (2014) 20-27.

[20] L. Li, Z. Chen, L. Song, M. Xu, H. Zhu, L. Gong, K. Zhang, Journal of Alloys and Compounds, 638 (2015) 77-82.

[21] J.-Z. Kong, C. Ren, G.-A. Tai, X. Zhang, A.-D. Li, D. Wu, H. Li, F. Zhou, Journal of Power Sources, 266 (2014) 433-439.

[22] S.U. Woo, C.S. Yoon, K. Amine, I. Belharouak, Y.K. Sun, Journal of The Electrochemical Society, 154 (2007) A1005-A1009.

[23] Y.K. Sun, S.W. Cho, S.W. Lee, C.S. Yoon, K. Amine, Journal of The Electrochemical Society, 154 (2007) A168-A172.

[24] K. Yang, L.-Z. Fan, J. Guo, X. Qu, Electrochimica Acta, 63 (2012) 363-368.

[25] B. Huang, X. Li, Z. Wang, H. Guo, Materials Letters, 131 (2014) 210-213.

[26] X. Ma, C. Wang, X. Han, J. Sun, Journal of Alloys and Compounds, 453 (2008) 352-355.

[27] G.-R. Hu, X.-R. Deng, Z.-D. Peng, K. Du, Electrochimica Acta, 53 (2008) 2567-2573.

[28] D. Wang, X. Li, Z. Wang, H. Guo, Z. Huang, L. Kong, J. Ru, Journal of Alloys and Compounds, 647 (2015) 612-619.

[29] D. Wang, X. Li, Z. Wang, H. Guo, X. Chen, X. Zheng, Y. Xu, J. Ru, Electrochimica Acta, 174 (2015) 1225-1233.

[30] Y. Liu, Q. Wang, Y. Lu, B. Yang, M. Su, Y. Gao, A. Dou, J. pan, Journal of Alloys and Compounds, 638 (2015) 1-6.

[31] Y. Huang, F.-M. Jin, F.-J. Chen, L. Chen, Journal of Power Sources, 256 (2014) 1-7.

[32] S. Patoux, C. Wurm, M. Morcrette, G. Rousse, C. Masquelier, Journal of Power Sources, 119 (2003) 278-284.

[33] L. Li, Z. Chen, Q. Zhang, M. Xu, X. Zhou, H. Zhu, K. Zhang, Journal of Materials Chemistry A, 3 (2015) 894-904.

[34] J. Chen, J. Xu, S. Zhou, N. Zhao, C.-P. Wong, Nano Energy, 15 (2015) 719-728.

[35] N. Liu, J. Shen, D. Liu, Electrochimica Acta, 97 (2013) 271-277.

[36] Z. Wang, E. Liu, C. He, C. Shi, J. Li, N. Zhao, Journal of Power Sources, 236 (2013) 25-32.

[37] Q.Y. Wang, J. Liu, A.V. Murugan, A. Manthiram, Journal of Materials Chemistry, 19 (2009) 4965-4972.

[38] X. Xiong, Z. Wang, G. Yan, H. Guo, X. Li, Journal of Power Sources, 245 (2014) 183-193.

[39] B. Huang, X. Li, Z. Wang, H. Guo, Z. He, R. Wang, J. Wang, X. Xiong, Materials Letters, 115 (2014) 49-52.

[40] J. Chong, S. Xun, X. Song, G. Liu, V.S. Battaglia, Nano Energy, 2 (2013) 283-293.

[41] L. Yang, T. Markmaitree, B.L. Lucht, Journal of Power Sources, 196 (2011) 2251-2254.

[42] G. Hu, M. Zhang, L. Wu, Z. Peng, K. Du, Y. Cao, Electrochimica Acta, 213 (2016) 547-556.

[43] J.-Z. Kong, S.-S. Wang, G.-A. Tai, L. Zhu, L.-G. Wang, H.-F. Zhai, D. Wu, A.-D. Li, H. Li, Journal of Alloys and Compounds, 657 (2016) 593-600.

[44] A.S. Andersson, B. Kalska, P. Eyob, D. Aernout, L. Haggstrom, J.O. Thomas, Solid State Ionics, 140 (2001) 63-70.

[45] C. Masquelier, A.K. Padhi, K.S. Nanjundaswamya, J.B. Goodenough, Journal of solid state chemistry, 135 (1998) 228-234.

[46] B. Huang, X. Li, Z. Wang, H. Guo, X. Xiong, J. Wang, Journal of Alloys and Compounds, 583 (2014) 313-319.

[47] D. Zhang, B.S. Haran, A. Durairajan, R.E. White, Y. Podrazhansky, B.N. Popov, Journal of Power Sources, 91 (2000) 122-129.

[48] J. Hong, H.-D. Lim, M. Lee, S.-W. Kim, H. Kim, S.-T. Oh, G.-C. Chung, K. Kang, Chemistry of Materials, 24 (2012) 2692-2697.

Figure captions

Fig. 1. XRD patterns of the as-prepared materials.

Fig. 2. SEM images of (a-c) NCM-LFP0, (d-f) NCM-LFP0.5, (g-i) NCM-LFP1, (j-l) NCM-LFP2 and (m-o) NCM-LFP3.

Fig. 3. EDS mapping for Fe and P of (a-c) NCM-LFP0.5, (d-f) NCM-LFP1, (g-i) NCM-LFP2 and (j-l) NCM-LFP3.

Fig. 4. (a-e) EDS spectra of the as-prepared materials, together with (f) the semi-quantitative analysis for Fe and P in them.

Fig. 5 XPS spectra of NCM-LFP0 and NCM-LFP1. (a) Ni 2p, (b) Co 2p, (c) Mn 2p, (d) Fe 2p (only for NCM-LFP1), (e) P 2p (only for NCM-LFP1), (f) C 1s.

Fig. 6. Initial charge-discharge curves (0.1 C) and cycling performances (1 C) of the as-prepared materials within the operating voltage windows of (a, c) 2.8-4.5 V and (b, d) 2.8-4.6 V

Fig. 7. Nyquist plots of (a) NCM-LFP0, (b) NCM-LFP0.5, (c) NCM-LFP1 (d) NCM-LFP2 and (e) NCM-LFP3 after 1 and 100 charge-discharge cycles at 1 C rate within the operating voltage window of 2.8-4.5 V, together with (f) the equivalent circuit used to simulate the data.

Fig. 8. Schematic diagram of the (a) coating process, together with the reactions occurred on the (b) uncoated and (c) coated particles.

Table caption

Table 1. Lattice parameters of the as-prepared materials.

Table 2. Calculated R_{sf} and R_{ct} values of the as-prepared samples after 1 cycle and 100 cycles.

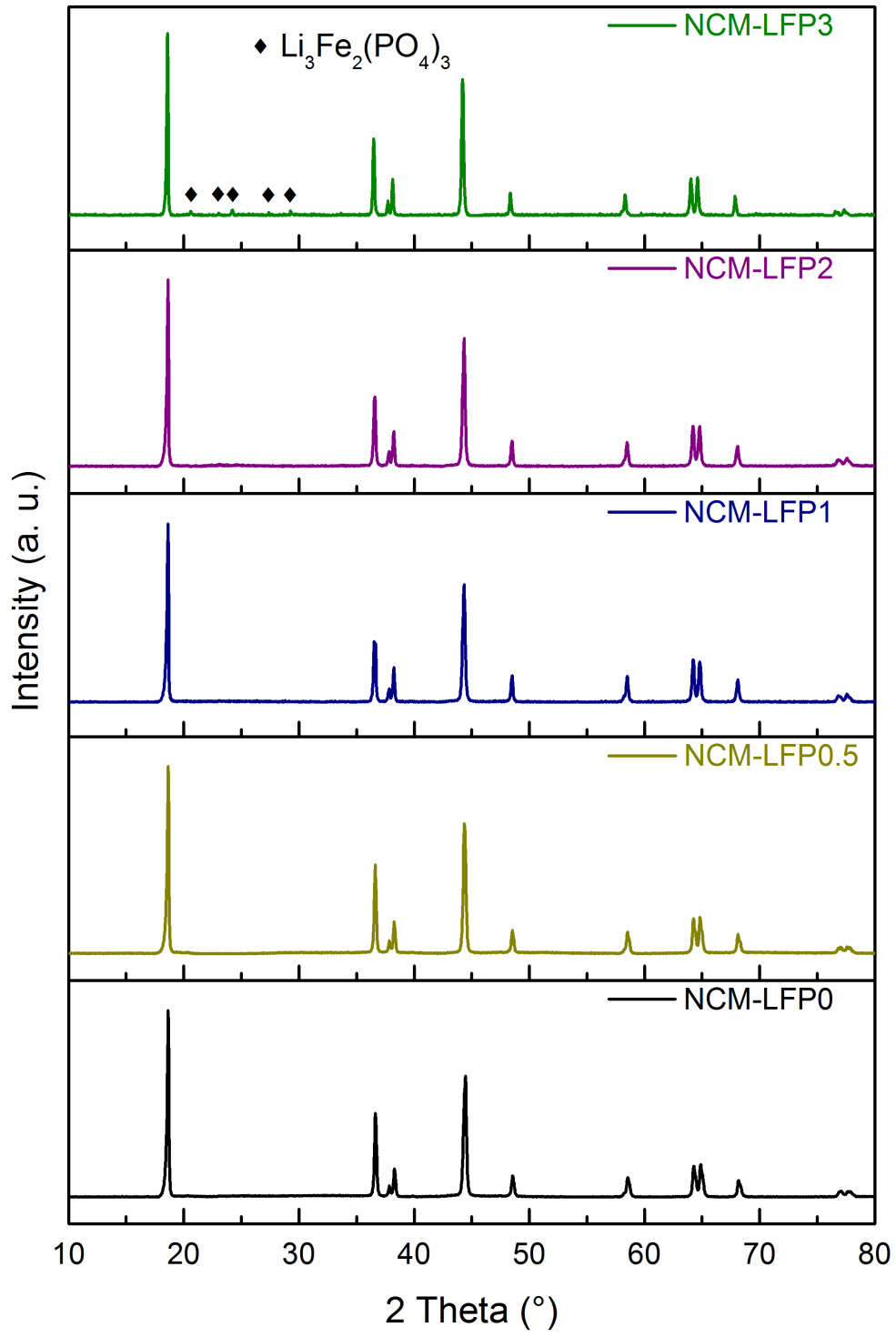

Fig. 1. XRD patterns of the as-prepared materials.

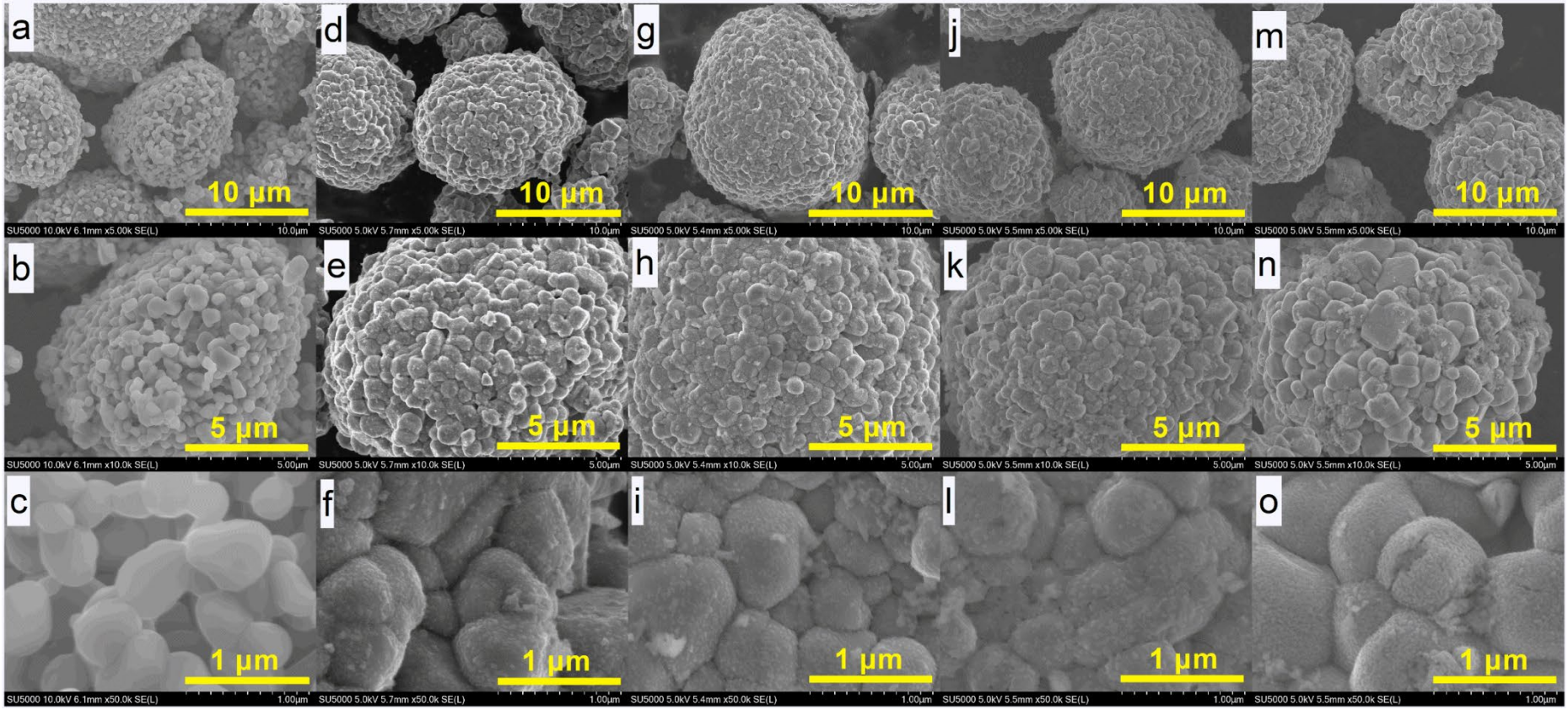

Fig. 2. SEM images of (a-c) NCM-LFP0, (d-f) NCM-LFP0.5, (g-i) NCM-LFP1, (j-l) NCM-LFP2 and (m-o) NCM-LFP3.

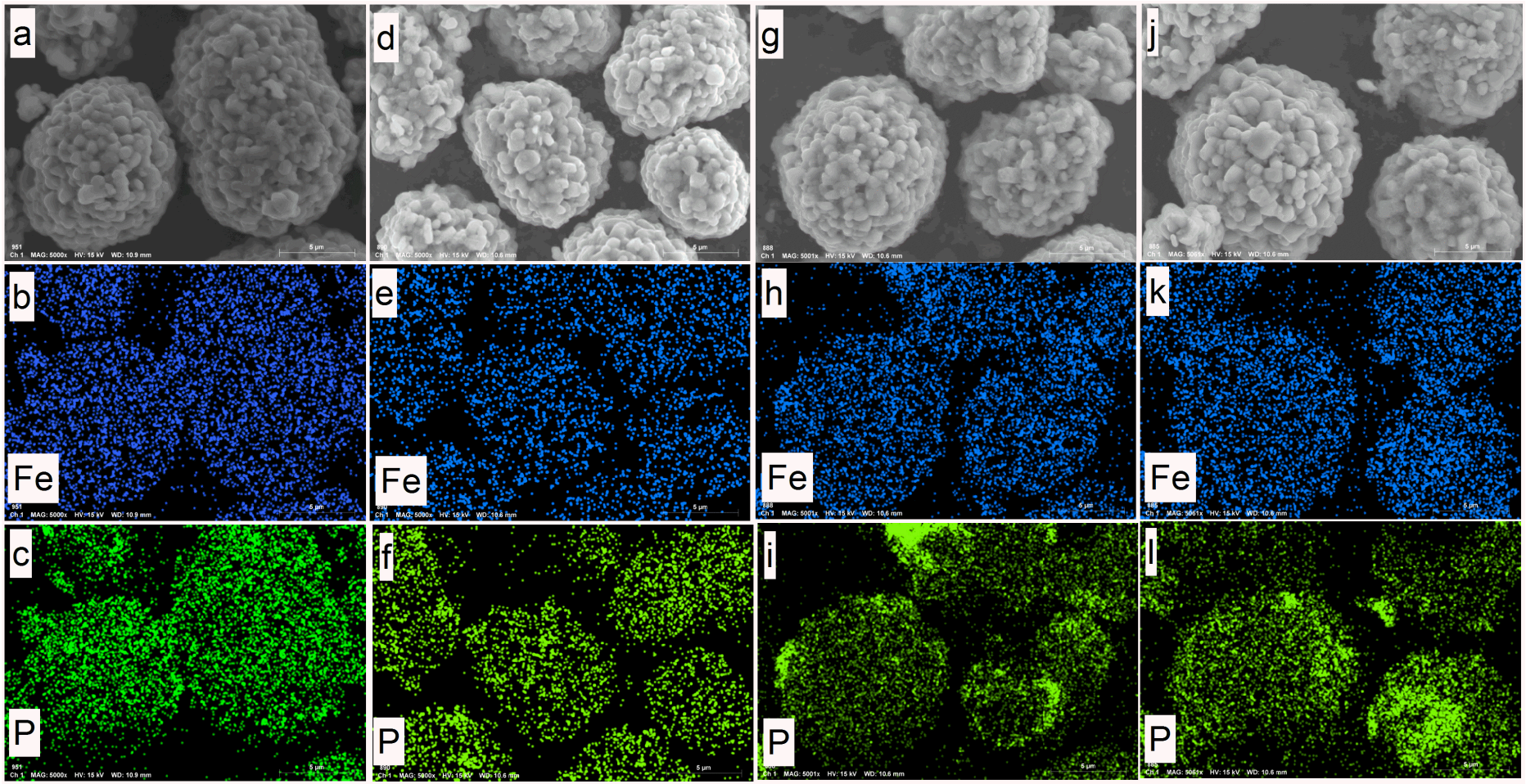

Fig. 3. EDS mapping for Fe and P of (a-c) NCM-LFP0.5, (d-f) NCM-LFP1, (g-i) NCM-LFP2 and (j-l) NCM-LFP3.

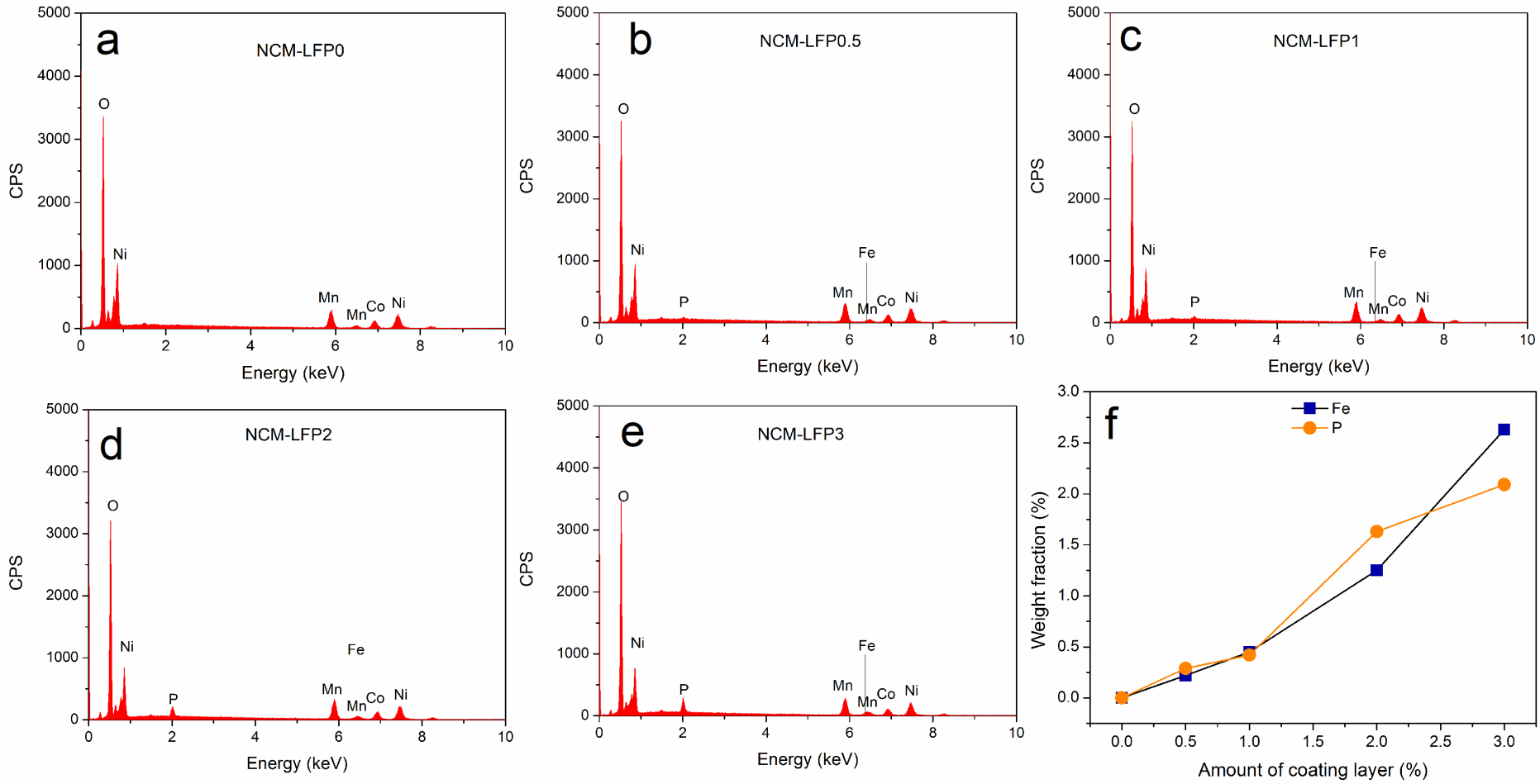

Fig. 4. (a-e) EDS spectra of the as-prepared materials, together with (f) the semi-quantitative analysis for Fe and P in them.

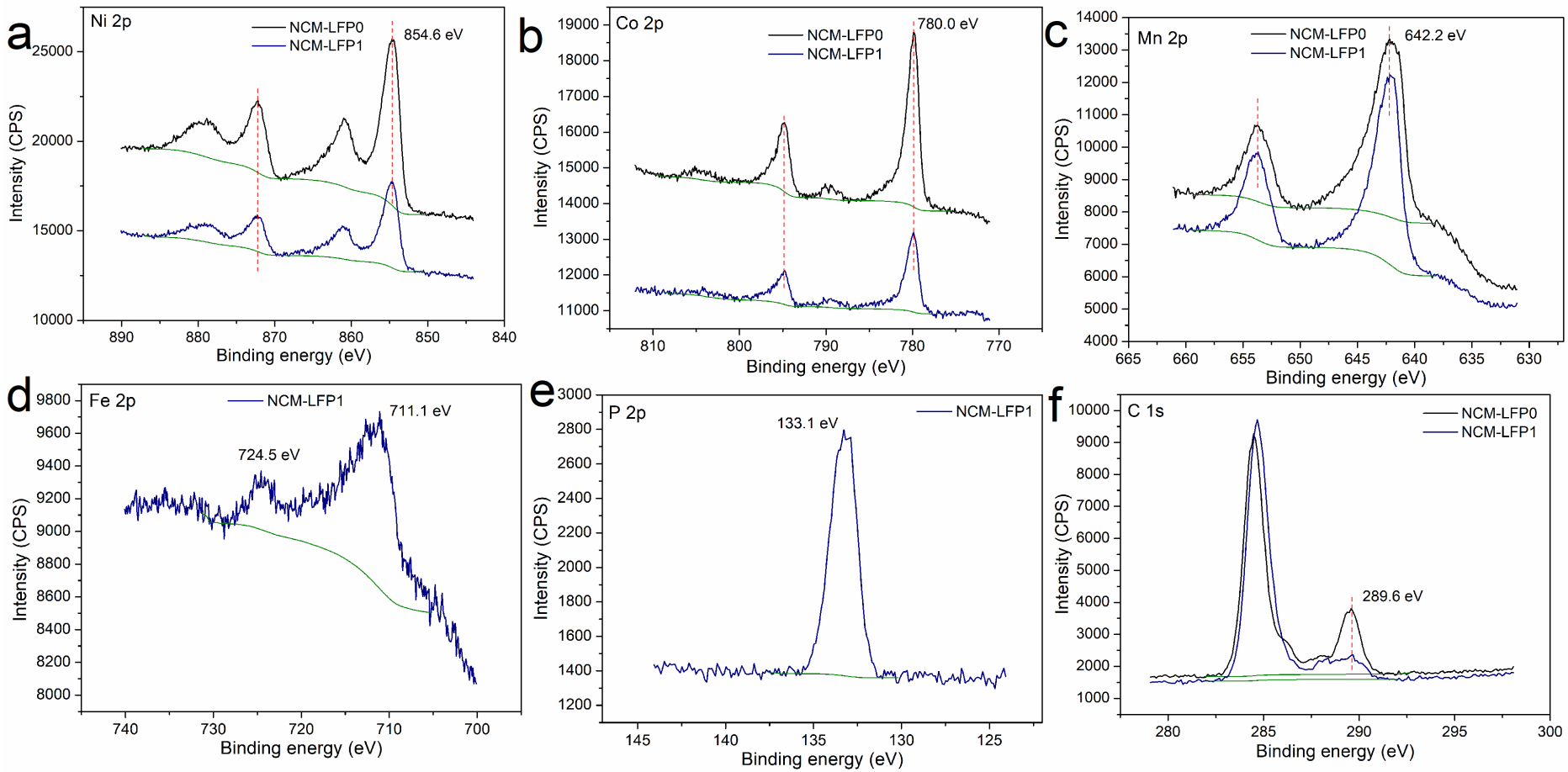

Fig. 5 XPS spectra of NCM-LFP0 and NCM-LFP1. (a) Ni 2p, (b) Co 2p, (c) Mn 2p, (d) Fe 2p (only for NCM-LFP1), (e) P 2p (only for NCM-LFP1), (f) C 1s.

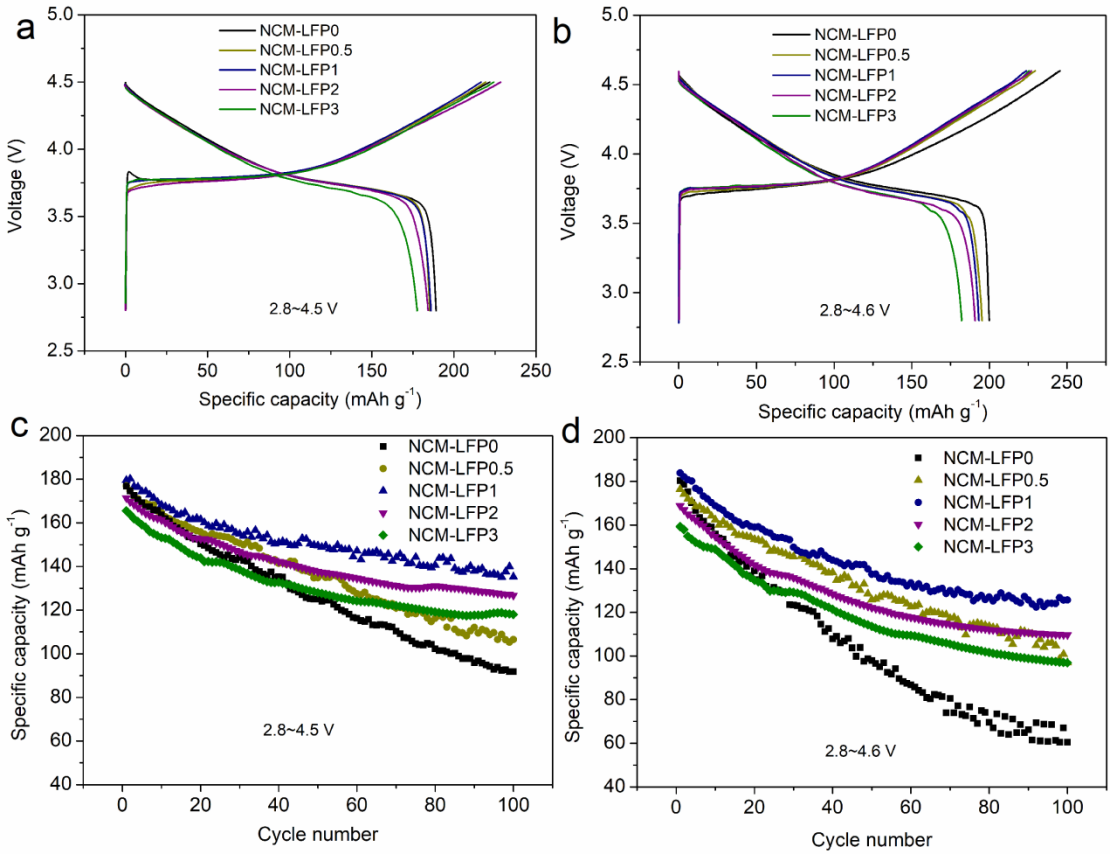

Fig. 6. Initial charge-discharge curves (0.1 C) and cycling performances (1 C) of the as-prepared materials within the operating voltage windows of (a, c) 2.8-4.5 V and (b, d) 2.8-4.6 V

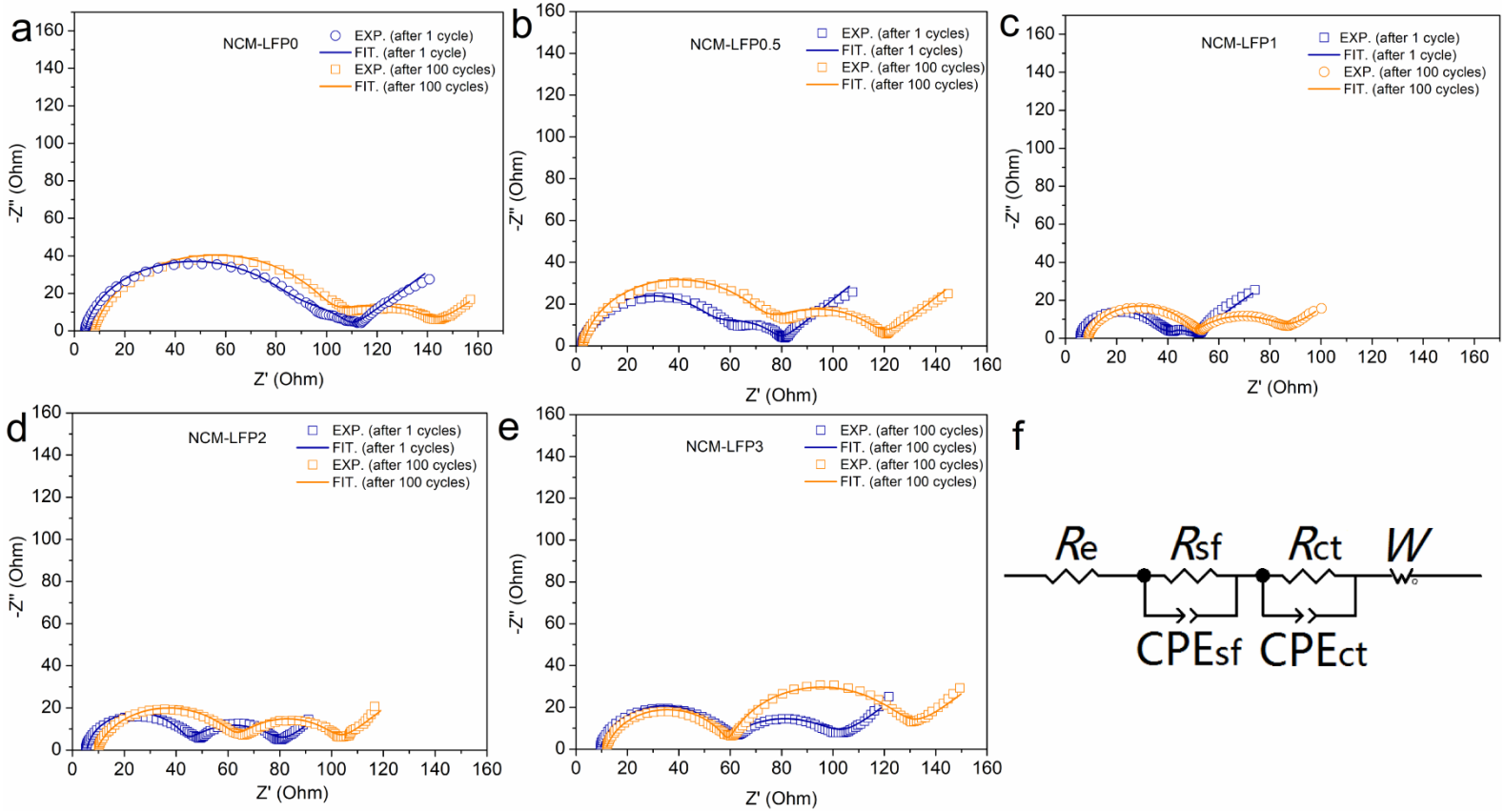

Fig. 7. Nyquist plots of (a) NCM-LFP0, (b) NCM-LFP0.5, (c) NCM-LFP1 (d) NCM-LFP2 and (e) NCM-LFP3 after 1 and 100 charge-discharge cycles at 1 C rate within the operating voltage window of 2.8-4.5 V, together with (f) the equivalent circuit used to simulate the data.

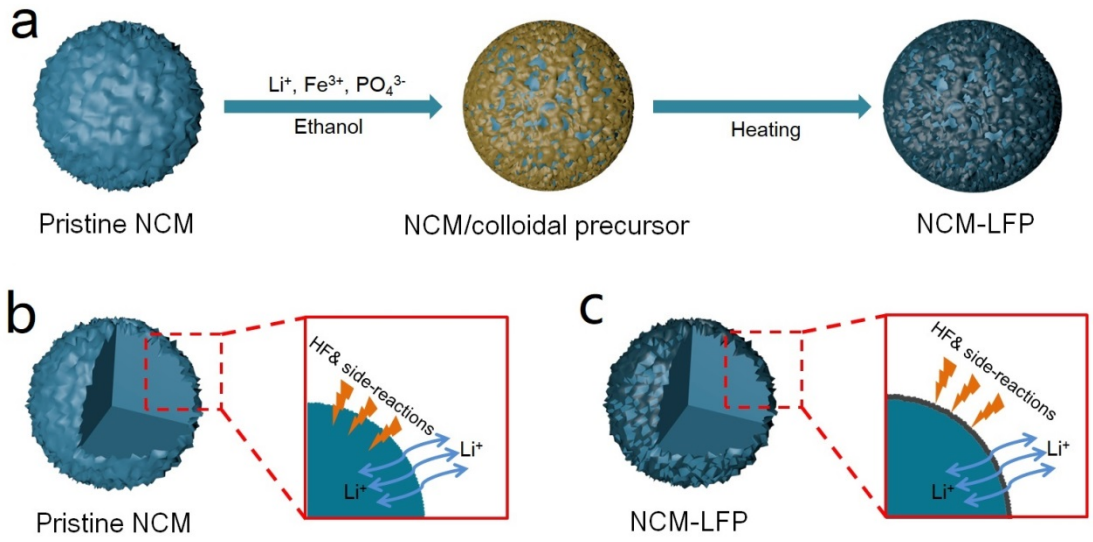

Fig. 8. Schematic diagram of the (a) coating process, together with the reactions occurred on the (b) uncoated and (c) coated particles.

Samples	Lattice parameters (Å)	
	a	*c*
NCM-LFP0	2.8733	14.2527
NCM-LFP0.5	2.8739	14.2522
NCM-LFP1	2.8735	14.2523
NCM-LFP2	2.8742	14.2517
NCM-LFP3	2.8740	14.2520

Table 1 Lattice parameters of the as-prepared materials.

Samples	R_{sf} (Ohm)		R_{ct} (Ohm)	
	1^{st}	100^{th}	1^{st}	100^{th}
NCM-LFP0	78.85	102.43	19.43	42.76
NCM-LFP0.5	49.38	69.73	26.13	44.78
NCM-LFP1	27.94	40.47	14.30	35.69
NCM-LFP2	34.09	37.42	27.78	53.97
NCM-LFP3	48.19	47.28	42.57	65.52

Table 2 Calculated R_{sf} and R_{ct} values of the as-prepared samples after 1 cycle and 100 cycles.